

# Optical properties, electronic structure and London dispersion interactions for nanostructured interfacial and surficial films

G.L. Tan<sup>a</sup>, Roger H. French<sup>a,b,\*</sup>

<sup>a</sup> Department of Materials Science and Engineering, University of Pennsylvania, Philadelphia, PA 19104, USA

<sup>b</sup> DuPont Co. Central Research, E356-384, Exp. Sta. Wilmington, DE 19880, USA

Received 29 July 2005; received in revised form 18 November 2005

## Abstract

Nanostructured amorphous films exhibit complex thermodynamic and kinetic behavior. To understand the structure and properties of nanostructured amorphous films in silicon based ceramics ( $\text{Si}_3\text{N}_4$ , SiC, Si) and in  $\text{SrTiO}_3$  ceramics, we have focused on experimental studies to determine the interband electronic structure and optical properties. We use vacuum ultraviolet spectroscopy for bulk materials, and valence electron energy loss spectroscopy (VEELS) in either transmission mode in the transmission electron microscope for interfacial films, and are developing VEELS in reflection mode for surficial films. These experimental data are quantitatively analyzed using Kramers–Kronig analysis to determine the complex optical properties of the constituent materials. This interband electronic structure information is the fundamental input to determine from Lifshitz theory the London dispersion interaction in these low-dimensional systems. We present interband transition strengths of  $\text{AlPO}_4$ ,  $\text{SiO}_2$  and rare-earth doped MgSiON glasses, and also of SiC and  $\text{SrTiO}_3$  and their grain boundaries. We use a new multilayer approach to produce graded interface models for the London dispersion interaction in complex nanostructured interfacial and surficial films.

© 2006 Elsevier B.V. All rights reserved.

**Keywords:** Optical properties; Electronic structure; London dispersion interaction; Van der Waals forces; Films; Interfacial; Surficial

## 1. Introduction

Nanostructured amorphous films, such as the intergranular glassy films seen in  $\text{Si}_3\text{N}_4$  ceramics, exhibit complex thermodynamic and kinetic behavior. These complex phases can arise at interfaces between two materials or at surfaces between one phase and a gas phase. Due to their nanometer scale and close proximity to other materials, their properties are not fully determined by bulk thermodynamics or kinetics, but are also a result of their composition and internal structure, and the composition and structure of the adjacent phases.

Understanding the structure and properties of nanostructured amorphous films in silicon based ceramics ( $\text{Si}_3\text{N}_4$ , SiC, Si) and in  $\text{SrTiO}_3$  ceramics at both interfaces and surfaces has been the focus of the Nanostructured Amorphous Films (NanoAM) project which has been funded by both the National Science Foundation of the United States of America (NSF Award DMR-0010062), and Cordis of the European Union Commission

(Contract G5RD-CT-2001-00586). This work has drawn upon a multidisciplinary team of scientists, both experimentalists and theorists, focused on a common set of materials and samples, with the goal of advancing our understanding and ability to control the unique structure and properties of these low-dimensional systems.

In our work we have focused on experimental studies to determine the interband electronic structure and optical properties of the films and substrate materials, using vacuum ultraviolet (VUV) spectroscopy [1], and valence electron energy loss spectroscopy (VEELS) in either transmission mode (TEELS) [2] in the transmission electron microscope, or in reflection mode (REELS). This interband electronic structure information is the fundamental input to determine from first principles one of the important thermodynamic interaction energies in these low-dimensional systems, the London dispersion interaction, a component of the van der Waals interaction.

We have made substantial progress in the development of experimental methods, determined quantitative optical properties and interband electronic structures for these materials and films, and made advances in our understanding and ability to address the relevance of the London dispersion interaction in these systems, such as the London dispersion interaction in

\* Corresponding author.

E-mail address: roger.h.french@usa.dupont.com (R.H. French).

URL: <http://www.lrsm.upenn.edu/~frenchrh/index.htm>.

atomically structured grain boundaries, and a gradient interface approach to calculating the London dispersion interaction for realistic systems. In this paper we review the progress made in experimental and analytical methods for understanding optical properties, electronic structure, and London dispersion interactions in nanostructured amorphous films at interfaces and surfaces, and review the results developed for a number of systems, including new results on  $\text{AlPO}_4$ ,  $\text{SiC}$  and  $\text{SiON}$  Glasses, and recent results on  $\text{SiO}_2$ ,  $\text{Si}_3\text{N}_4$  and  $\text{SrTiO}_3$ .

## 2. Methods

Three experimental methods have been used to determine the quantitative optical properties and interband electronic structure of bulk, interfacial and surficial materials. Due to the differences in the configurations of these three materials, different methods are best suited to each. For example, VUV reflectance spectroscopy is capable of determining the properties of bulk homogenous samples of a material, and due to its inherently high energy resolution, serves to provide the basic reference spectra for the bulk electronic structure of materials. For nanometer scale interfacial or intergranular materials, the use of VEELS in transmission mode in the analytical transmission electron microscopy (TEM) is best suited due to its high lateral spatial resolution. For nanometer scale surficial films, VEELS in reflection mode is best suited due to its high surface sensitivity.

### 2.1. Experimental

#### 2.1.1. Vacuum ultraviolet reflectance spectroscopy

VUV spectroscopy has become an established technique for electronic structure studies of bulk materials [1,3–7]. It has the advantage of covering the complete energy range of the valence interband transitions and is not plagued by the sample charging that attends photoelectron spectroscopy on insulators. The VUV spectrophotometer, whose details have been published previously [8–11], includes a laser plasma light source, a monochromator, filters and a multichannel detector. The light source is not polarized, and the incident angle of the light on the sample is near normal. The energy range of the instrument is from 1.7 to 44 eV, or from 700 to 28 nm, which allows us to extend beyond the air-cutoff of 6 eV and the window-cutoff 10 eV. The resolution of the instrument is 0.2 to 0.6 nm, which corresponds to 16 meV resolution at 10 eV or 200 meV resolution at 35 eV.

#### 2.1.2. Valence electron energy loss spectroscopy

Electron energy loss spectroscopy (EELS), the second experimental method, uses the electromagnetic interaction of incident electrons to probe the electron energy loss function (ELF), another form of the complex optical properties of a material. EELS spectroscopy can be performed as a transmission (TEELS) or reflection (REELS) measurement. Spatially resolved valence TEELS (V-TEELS) probes internal interfaces and films while valence REELS (V-REELS) can provide information on surficial films. Once acquired, the experimental energy loss function must be analyzed taking into consideration the relative contributions of the “Bulk”  $\text{ELF} = -\text{Im}[1/\epsilon]$  [12]

and/or the “Surface”  $\text{ELF} = -\text{Im}[1/(\epsilon + 1)]$  [13] to the experimentally acquired spectra, and then Kramers–Kronig analysis is used to extract the complex dielectric function of the materials under study.

**2.1.2.1. Transmission VEELS.** V-TEELS measurements [2,7] are becoming a standard method in analytical microscopy and in this work were performed using a Gatan parallel electron energy-loss spectrometer attached to a VG Microscopes HB501 UX dedicated STEM [2,7,14]. In this instrument the energy resolution is better than 0.6 eV, measured by the full width at half maximum of the zero-loss peak. The spatial resolution of the measurement is determined by the electron probe size and was well below 0.4–0.6 nm.

V-TEELS spectra are typically acquired using an energy dispersion of 0.1 eV/channel to record spectra up to energy-losses higher than 90 eV. We acquire one hundred single spectra across the internal interface of interest, spatially over sampling the interface, using scan lengths typically between 12.5 and 40 nm. Therefore, the spatial separation of two adjacent spectra in the line scan is between 0.125 and 0.4 nm. This approach provides for the determination of very local changes within the acquired electron energy loss spectra.

**2.1.2.2. Reflection VEELS.** When the sample under study is a surficial film on a substrate, VUV optical measurements are not well-suited because both the film and the substrate are probed, due to the large optical probing depth in the VUV (which can vary from 100 nm to centimeter depths). Instead V-REELS [15], a method often used in the surface science community, could provide better quantitative electronic structure information if the necessary quantitative analysis could be developed. We therefore have taken the first steps in this development. V-REELS data are acquired using low-energy electrons (with primary beam energies from 200 to 1500 eV), and then the energy loss spectra are accumulated in the energy range from 0 to 150 eV in reflection mode. Due to the small inelastic mean free path (IMFP) of electrons, which determines the probing depth, only the surficial film will be probed if the electron energy is low enough that the IMFP is smaller than the thickness of the thin films. To realize the opportunities of V-REELS in optical property and electronic structure studies, the experimentally acquired electron energy loss function must be modeled for the relative contribution of bulk and surface energy loss excitations, and then Kramers–Kronig analysis of the two ELF's can be achieved. This modeling of the V-REELS bulk and surface interactions is a focus of our future work.

### 2.2. Analytical procedures

#### 2.2.1. Kramers–Kronig analysis

The propagation of electromagnetic waves in materials is governed by Maxwell's equations and the optical properties of solids are the fundamental materials input [16]. These optical properties are complex quantities in which the real and imaginary parts correspond to absorption and dispersion of light in the material. The dispersion of light is the change of the

wavelength and speed of propagating light under the influence of the real part of the index of refraction of a material. There are algebraic relations among the numerous optical properties, such as the index of refraction ( $\hat{n} = n + ik$ ), dielectric constant ( $\hat{\epsilon} = \epsilon_1 + i\epsilon_2$ ), optical conductivity ( $\hat{\sigma} = \sigma_1 + i\sigma_2$ ) and interband transition strength ( $\hat{J}_{cv} = J_{cv,1} + iJ_{cv,2}$ ). In addition, the Kramers–Kronig dispersion relations govern the relationship of the real and imaginary components of any one optical property. Here we use the form presented by Wooten [16] for optical property relations, and NIST [17] for fundamental physical constants.

The Kramers–Kronig dispersion relations [18–20] permit the analysis of reflectance, or other optical, data to obtain any conjugate pair of complex optical properties. The experimental data must span an infinite energy range and since, in practice, experimental data are of limited range, these must be extended by extrapolation.

**2.2.1.1. Analysis of the reflectance.** The measured optical reflectance of  $\text{AlPO}_4$  is shown in Fig. 1 as measured from a single crystal sample using VUV reflectance spectroscopy. For the optical reflectance,  $R(E)$ , and the reflected amplitude,  $\rho(E) = \sqrt{R(E)}$ , the Kramers–Kronig transform for reflectance [21] recovers the phase  $\theta(E)$  of the reflected wave:

$$\theta(E) = -\frac{2E}{\pi} P \int_0^{\infty} \frac{\ln\{\rho(E')\}}{E'^2 - E^2} dE' \quad (1)$$

Here  $P$  denotes the Cauchy principal part of the integral, avoiding the pole at  $E = E'$ . To perform this Kramers–Kronig transform, we use Fast Fourier Transforms to expedite the integrations and also combine the low-energy data extrapolation through the vis-

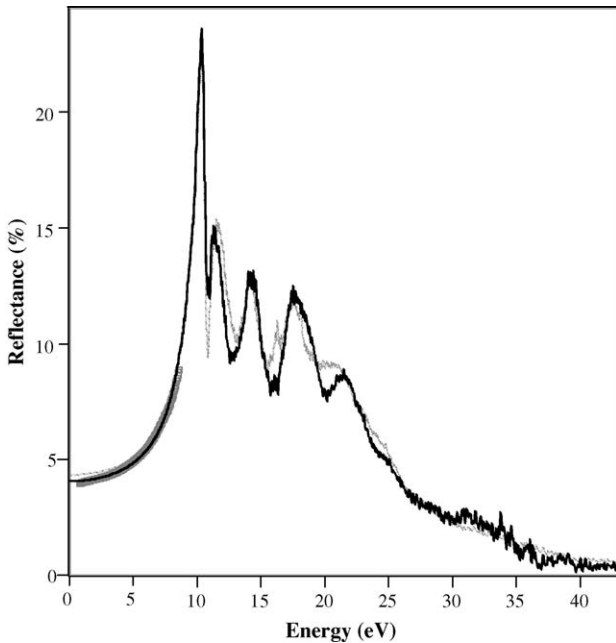


Fig. 1. Reflectance of crystalline  $\text{AlPO}_4$  (black line) compared with crystalline  $\text{SiO}_2$  (grey line) as measured using VUV spectroscopy. In addition the reflectance of crystalline  $\text{AlPO}_4$  as calculated from spectroscopic ellipsometry below 8 eV is shown as the wide grey line.

ible region by augmentation with spectroscopic ellipsometry data. The details of these methods are discussed in detail in the Kramers–Kronig Analysis Appendix of our 1999 paper [22]. Once the reflected amplitude and phase have been determined, any conjugate pair of optical properties can be computed from the relations in Section 2.2.2.

### 2.2.1.2. Analysis of the energy loss functions.

**2.2.1.2.1. Bulk energy loss function.** Kramers–Kronig analysis of electron energy loss function measurements in the transmission mode (TEELS) using high-energy electrons is a well-established method [12,23–25] to determine the optical properties of a solid over a wide energy range. Within the range of validity of the dielectric theory [26,27], the probability that an electron traveling in a medium of dielectric function  $\epsilon(\mathbf{q}, E)$ , suffering an inelastic scattering process characterized by a momentum transfer  $\mathbf{q}$  and an energy loss  $E$ , is determined by the energy loss function (ELF)  $\text{Im}[-1/\epsilon(\mathbf{q}, E)]$ . Within the optical limit ( $\mathbf{q} \rightarrow 0$ ) both the transverse and longitudinal dielectric constant ( $\epsilon(\mathbf{0}, E)$ ) coincide [24] so that the TEELS spectra will approach the optical energy loss function  $\text{Im}[-1/\epsilon(\mathbf{0}, E)]$ . Thus, the Kramers–Kronig analysis enables the determination of optical properties. In the following, we denote the energy loss either by  $E$  or by  $\hbar\omega$ .

As the dielectric response function is causal, a Kramers–Kronig transformation can be used to derive the function  $\text{Re}[1/\epsilon(\omega)]$  from  $\text{Im}[-1/\epsilon(\omega)]$ :

$$\text{Re} \left[ \frac{1}{\epsilon(\omega)} \right] - 1 = -\frac{2}{\pi} P \int_0^{\infty} \text{Im} \left[ -\frac{1}{\epsilon(\omega')} \right] \frac{\omega' d\omega'}{\omega'^2 - \omega^2} \quad (2)$$

$$\text{Im} \left[ -\frac{1}{\epsilon(\omega)} \right] = \omega \frac{2}{\pi} P \int_0^{\infty} \frac{\text{Re} \left[ \frac{1}{\epsilon(\omega')} \right] - 1}{\omega'^2 - \omega^2} d\omega' \quad (3)$$

In Eqs. (2) and (3), the factor  $\omega' / (\omega'^2 - \omega^2)$  acts as a “weighting function”, giving prominence to energy losses  $\hbar\omega'$  which lie close to  $\hbar\omega$ .

$\text{Im}[-1/\epsilon]$  is given an absolute scale by use of a Kramers–Kronig sum rule, the index sum rule, obtained by setting  $\omega = 0$  in Eq. (2):

$$\begin{aligned} 1 - \text{Re} \left[ \frac{1}{\epsilon(0)} \right] &= \frac{2}{\pi} \int \text{Im} \left[ -\frac{1}{\epsilon(\omega)} \right] \frac{d\omega}{\omega} \\ &= \frac{2}{\pi} \int [\text{scale\_factor} \times \text{data}] \frac{d\omega}{\omega} \end{aligned} \quad (4)$$

Since  $\text{Re}[1/\epsilon(0)] = \epsilon_1 / (\epsilon_1^2 + \epsilon_2^2)$ , the left-hand side of Eq. (4) can be taken as unity for a metal, where both  $\epsilon_1$  and  $\epsilon_2$  become very large at  $\omega \rightarrow 0$ . In case of an insulator,  $\epsilon_2$  is small for small  $\omega$  and  $\text{Re}[1/\epsilon(0)] \cong 1/\epsilon_1(0)$ , where  $\epsilon_1(0)$  is the square of the refractive index for visible light.

**2.2.1.2.2. Surface energy loss function.** The surficial optical properties and interband electronic structure and properties of the surficial films could be determined from REELS if one could quantitatively analyze the experimentally acquired energy loss function to determine how much the surface ELF and the bulk ELF each contribute to the V-REELS spectrum.

The first problem one encounters in this endeavor is that the Kramers–Kronig transform of a pure surface energy loss function has not been previously reported.

We have developed the Kramers–Kronig dispersion relationship for the pure surface energy loss function to derive the real part of  $[1/(\varepsilon(\omega) + 1)]$  and then the complex dielectric function  $\varepsilon(\omega)$  [13]. The new Kramers–Kronig dispersion relationship is directly applicable to very low-energy REELS spectra, based on the assumption that one can derive a pure surface energy loss function from experimental REELS spectra at very low energy, a task that we are also currently pursuing. We then would use Kramers–Kronig analysis upon this surface energy loss function to derive the conjugate part of the surface loss function and subsequently, the complex dielectric functions and optical constants. This represents an approach to determine the electronic structure and physical properties of surficial films from REELS spectra using the new surface Kramers–Kronig transform. A main assumption is that the pure surface energy loss function could be separated from the bulk one in the experimental V-REELS spectrum. The result would be a good approximation of the dielectric function of a surficial film whose thickness is less than the inelastic mean free path (IMPF) of the electrons in REELS.

The Kramers–Kronig dispersion relationship for the transformation of surface energy loss function is expressed in the following equations:

$$\begin{aligned} \operatorname{Re} \left[ \frac{1}{\varepsilon(\omega) + 1} \right] - \frac{1}{2} \\ = -\frac{2}{\pi} P \int_0^{\infty} \operatorname{Im} \left[ -\frac{1}{\varepsilon(\omega') + 1} \right] \frac{\omega'}{\omega'^2 - \omega^2} d\omega' \end{aligned} \quad (5)$$

$$\operatorname{Im} \left[ -\frac{1}{\varepsilon(\omega) + 1} \right] = \omega \frac{2}{\pi} P \int_0^{\infty} \frac{\operatorname{Re} \left[ \frac{1}{\varepsilon(\omega') + 1} \right] - \frac{1}{2}}{\omega'^2 - \omega^2} d\omega' \quad (6)$$

The input surface energy loss function is given an absolute scaling according to the following index sum rule, which is comparable to the bulk index sum rule in Eq. (4). The surface index sum rule is

$$\begin{aligned} \frac{1}{2} - \operatorname{Re} \left[ \frac{1}{\varepsilon(0) + 1} \right] &= \frac{2}{\pi} \int \operatorname{Im} \left[ -\frac{1}{\varepsilon(\omega) + 1} \right] \frac{d\omega}{\omega} \\ &= \frac{2}{\pi} \int [\text{scale\_factor} \times \text{data}] \frac{d\omega}{\omega} \end{aligned} \quad (7)$$

### 2.2.2. Optical property relations

Once a conjugate pair of optical properties have been determined, such as the reflectance and the reflected phase, then the complex index of refraction, for example, is obtained by solving Eq. (8) and the dielectric function is obtained by Eq. (9):

$$\frac{n - 1 + ik}{n + 1 + ik} = \rho(E) e^{i\theta(E)} \quad (8)$$

$$\varepsilon_1 + i\varepsilon_2 = (n + ik)^2 \quad (9)$$

We typically render the optical response in terms of the complex quantity, the interband transition strength,  $J_{cv}(E)$ , which is related to  $\varepsilon(\omega)$  by

$$J_{cv} = J_{cv1} + iJ_{cv2} = \frac{m_0^2}{e^2 \hbar^2} \frac{E^2}{8\pi^2} (\varepsilon_2(E) + i\varepsilon_1(E)) \quad (10)$$

where  $m_0$  is the electron mass,  $e$  its charge and  $E$  is the energy.  $J_{cv}(E)$  is proportional to the interband transition probability and has units of  $\text{g cm}^{-3}$ . For computational convenience we take the prefactor  $m_0^2 e^{-2} \hbar^{-2}$  in Eq. (10), whose value in cgs-units is  $8.289 \times 10^{-6} \text{ g cm}^{-3} \text{ eV}^{-2}$ , as unity. Therefore, the units of the  $J_{cv}(E)$  spectra are  $(\text{eV}^2)$ .  $J_{cv1}$  (the real part of  $J_{cv}$ ) corresponds to the joint densities of states and  $J_{cv}$  is proportional to  $E^2 \varepsilon^*$ , where  $\varepsilon^*$  is the complex conjugate of  $\varepsilon$  [1]. The interband transition strength of  $\text{AlPO}_4$  and, for comparison, crystalline  $\text{SiO}_2$  (Quartz) as determined from Kramers–Kronig analysis of VUV reflectance are shown in Fig. 2. The similarities and differences in the interatomic bond energies in these two materials will be discussed in Sections 3.1 and 3.2.

With Kramers–Kronig analysis of the surface energy loss function, the determination of the complex dielectric function  $\varepsilon(\omega)$  is easily obtained from  $\operatorname{Re}[-1/(1 + \varepsilon(\omega))]$  and  $\operatorname{Im}[-1/(1 + \varepsilon(\omega))]$  as follows:

$$\varepsilon(\omega) = \varepsilon_1(\omega) + i\varepsilon_2(\omega) \quad (11)$$

$$\varepsilon_1(\omega) + 1 = \frac{-\operatorname{Re} \left[ -\frac{1}{1 + \varepsilon(\omega)} \right]}{\left\{ \operatorname{Re} \left[ -\frac{1}{1 + \varepsilon(\omega)} \right] \right\}^2 + \left\{ \operatorname{Im} \left[ -\frac{1}{1 + \varepsilon(\omega)} \right] \right\}^2} \quad (12)$$

$$\varepsilon_2(\omega) + 1 = \frac{\operatorname{Im} \left[ -\frac{1}{1 + \varepsilon(\omega)} \right]}{\left\{ \operatorname{Re} \left[ -\frac{1}{1 + \varepsilon(\omega)} \right] \right\}^2 + \left\{ \operatorname{Im} \left[ -\frac{1}{1 + \varepsilon(\omega)} \right] \right\}^2} \quad (13)$$

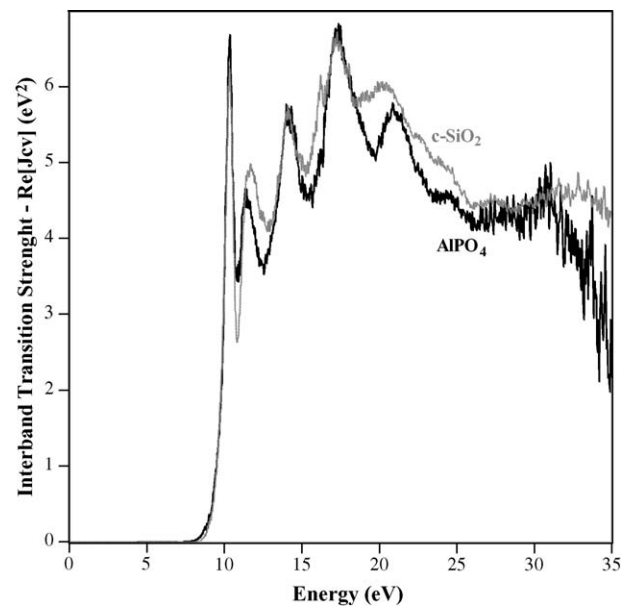


Fig. 2. Real part of the interband transition strength ( $\operatorname{Re}[J_{cv}]$ ) of crystalline  $\text{AlPO}_4$  (black line) compared with crystalline  $\text{SiO}_2$  (grey line) determined from Kramers–Kronig analysis of VUV reflectance data.

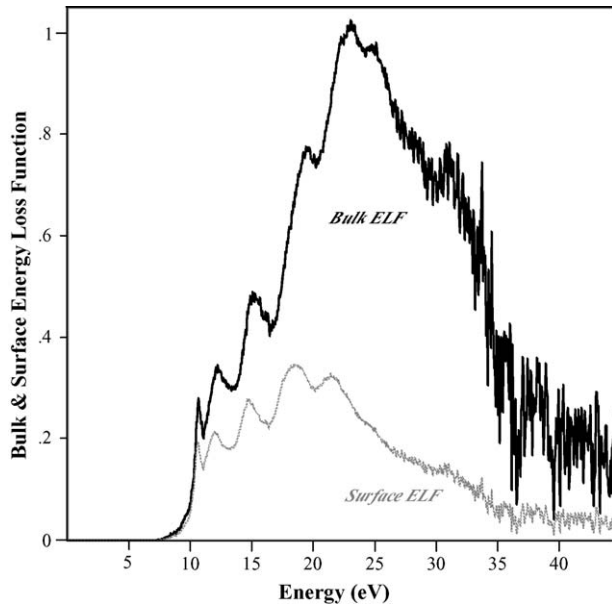


Fig. 3. Bulk electron energy loss function,  $-\text{Im}(1/\epsilon)$ , of crystalline  $\text{AlPO}_4$  (black line), showing a bulk plasmon resonance peak at 23.7 eV compared with the surface energy loss function,  $-\text{Im}(1/(\epsilon + 1))$  (grey line).

The dielectric function is calculated in a similar manner when the bulk energy loss function and its conjugate have been determined from Kramers–Kronig analysis of the VUV reflectance. Using these relations we show the bulk and surface energy loss functions for  $\text{AlPO}_4$  in Fig. 3. These will be discussed in Section 3.1.

With the complex optical properties of the material determined, such as its interband transition strength, we can then use the optical sum rules on these properties to determine additional information. For example, the oscillator strength sum rule [28,29] for the interband transition strength,  $n_{\text{eff}}(E)$ :

$$n_{\text{eff}}(E) = \frac{4v_f}{m_0} \int_0^E \frac{J_{\text{cv}}(E')}{E'} dE' \quad (14)$$

where  $v_f$  is the volume of the formula unit, gives the number of electrons contributing to the optical transitions up to an energy  $E$ . The results for  $\text{AlPO}_4$  are shown in Fig. 4 with  $v_f$ , the volume of the  $\text{AlPO}_4$  crystal formula unit, taken as 77.87 Å [1]. These results will be discussed in Section 3.1.

### 2.2.3. Calculation of Hamaker coefficients for the London dispersion interaction

Once the electronic structure of the bulk, interfacial or surficial material has been determined, then the full spectral Hamaker constant (where the thickness of the variational layer is approximately zero) or the full spectral Hamaker coefficient (which varies with, and is dependent on, thickness) [30] determines the magnitude of the van der Waals attraction between two materials, and can be determined using the Lifshitz methods [31,32]. When the interaction distances are small and the layer structure is simple, the London dispersion interaction can be calculated in the non-retarded limit because we can neglect the effects of the speed of light on the transit time of the virtual photon exchange

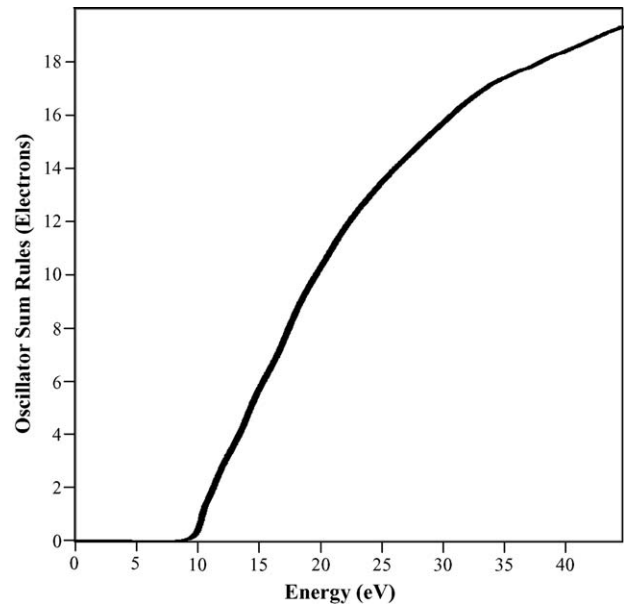


Fig. 4. Oscillator strength, or  $f$ , sum rule for crystalline  $\text{AlPO}_4$ .

among the materials. If the layer structure is more complex than the typical three layers or if the separations are greater than a few nanometers (where the effects of retardation can become large) it is important to explicitly include the effects of the speed of light and the complexity of the configuration on the dispersion interaction, and to represent the result as the thickness dependent Hamaker coefficient. The thickness dependent Hamaker coefficient contain more information, and can capture the effects of both retardation and of complex (multilayer) configurations. In the simple limit of a three-layer configuration, and with zero thickness of the varying layer, the Hamaker coefficient reduces to the Hamaker constant.

To calculate the London dispersion interaction and its non-retarded Hamaker constant we utilize another Kramers–Kronig dispersion relation to produce the London dispersion spectrum,  $\epsilon(i\xi)$ , which is an integral transform of the imaginary part of the dielectric constant from the real frequency  $\omega$  to the imaginary frequency  $i\xi$ . The London dispersion spectrum is a material's property and represents the retardation of the oscillators:

$$\epsilon(i\xi) = 1 + \frac{2}{\pi} \int_0^\infty \frac{\omega \epsilon_2(\omega)}{\omega^2 + \xi^2} d\omega \quad (15)$$

Once the complex optical properties as a function of the real frequency  $\omega$  have been determined, the London dispersion (LD) integral transform (Eq. (15)) must be applied to determine the London dispersion spectrum. The LD transform requires data over an infinite frequency or energy range, therefore we again use analytical extension or wings to continue the data beyond the experimental range. We choose power law wings of the form  $\text{Re}[J_{\text{cv}}] \propto \omega^{-\alpha}$  on the low energy side of the data and  $\text{Re}[J_{\text{cv}}] \propto \omega^{-\beta}$  on the high energy side of the data. We have chosen fixed values of  $\beta=3$  and  $\alpha=3$ . The detailed methods for calculating the full spectral Hamaker constant can be found in French's review article [30]. Once the London dispersion spectra of the two materials are determined,

the Hamaker constant is calculated using integrals of spectral differences.

**2.2.3.1. Three-layer Hamaker coefficients.** When two grains of material 1 are separated from each other by one unique intervening material 2, the non-retarded Hamaker constant,  $A_{121}^{\text{NR}}$ , can be calculated following Ninham and Parsegian [33,30]:

$$A_{121}^{\text{NR}} = -12\pi L^2 E_{\text{London}} \quad (16)$$

$E_{\text{London}}$ , the London dispersion free energy per unit surface area of the layer configuration, is obtained as follows:

$$E_{\text{London}} = \frac{\hbar}{4\pi^2} \int_0^\infty \rho \, d\rho \int_0^\infty \ln G(i\xi) \, d\xi \quad (17)$$

$$G_{121}^{\text{NR}}(i\xi) = 1 - \Delta_{12}^2(i\xi) \exp(-2b\rho) \quad (18)$$

where  $G$  is a function of  $\Delta$ , the difference of the London dispersion spectra on the two sides of any interface, and  $b$  is the thickness of the central layer. Thus,  $\Delta_{12}$  for the interface between materials 1 and 2 is

$$\Delta_{12}(i\xi) = \frac{\varepsilon_2(i\xi) - \varepsilon_1(i\xi)}{\varepsilon_2(i\xi) + \varepsilon_1(i\xi)} \quad (19)$$

**2.2.3.2. Multi-layer Hamaker coefficients.** A simple three-layer model ( $A_{123}$  for example) may not be sufficient to represent the more complex situations which arise in interfacial or surficial films or grain boundaries. For these, a multilayer model is used, which allows the introduction of more realistic graded properties instead of the simplistic abrupt property changes at the two interfaces of a 123 model. Due to the changes in the electronic structure and optical properties (such as the index of refraction) progressing across the interface, there are changes in the London dispersion spectra in the multilayer model as a function of position across the interface, and this graded optical contrast at the interface gives rise to the London dispersion interaction of Lifshitz theory. We can change the thickness and composition of each individual layer in the multilayer calculation to predict the Hamaker coefficient for arbitrarily complex interfaces [33a].

### 3. Results

Here we will use  $\text{AlPO}_4$  (Section 3.1), which is structurally comparable to  $\text{SiO}_2$ , as an example of the determination of the interband electronic structure of a material. These results will be compared to  $\text{SiO}_2$  in Section 3.2. We then discuss the interband electronic structure for new results on  $\text{SiC}$  (Section 3.3) and our prior results on  $\text{Si}_3\text{N}_4$  (Section 3.4) since these demonstrate the dissimilarities among these Si containing materials.  $\text{Si}_3\text{N}_4$  is also the reference material to consider when we discuss the new results on silicon oxynitride glasses (Section 3.5) which are similar to intergranular glassy films in silicon nitride ceramics. We then finish with recent advances (Section 3.6) we have made on graded interface models of grain boundaries, applied to  $\text{SrTiO}_3$  and its grain boundaries.

#### 3.1. $\text{AlPO}_4$

$\text{AlPO}_4$ , a rare phosphate named Berlinite, belongs to a class of *iso*-structural compounds  $\text{MXO}_4$  ( $M = \text{Si, Ge, Al, Ga, \dots}$  and  $X = \text{Si, Ge, P, As, \dots}$ ) which crystallize, at ambient pressures, in the trigonal phase (space group  $P3_221$ ), adopting structures made up of  $\text{MO}_4$  and  $\text{XO}_4$  tetrahedra and share quartz's structure as determined by a single crystal X-ray diffractometer [34]. That means quartz and  $\text{AlPO}_4$  have the same structure although the two minerals have rather different chemistries. Quartz,  $\text{SiO}_2$ , seems to be very different from Berlinite,  $\text{AlPO}_4$ . But if the formula of quartz is written as  $\text{SiSiO}_4$  then the similarity is obvious. The reason that Berlinite is able to have the same structure as quartz is because the aluminum and phosphorus ions are of similar size to silicon ions and thus can completely replace the silicon ions. It is  $\text{SiO}_4$  and  $\text{PO}_4$  tetrahedrons, respectively, which compose the similar structural units in small dimension for  $\text{SiO}_2$  and  $\text{AlPO}_4$ , and determine their electronic structures and most of the optical characterizations [36]. Therefore, the similarity of the optical properties between  $\text{SiO}_2$  and  $\text{AlPO}_4$ , seen in the interband transition strength spectra in Fig. 2, arises from their similar structural units  $-\text{SiO}_4$  or  $\text{PO}_4$  tetrahedrons and same crystal structure.

The interband transition strength spectrum for  $\text{AlPO}_4$  crystal [35] is shown in Fig. 2 and was derived from Kramers–Kronig analysis of the VUV reflectance spectrum of Fig. 1. Features in the interband transition strength are located at 10.4, 11.4, 14.2, 16.2, 17.3, 20.9, 22.5, 24.5, 28.0 and 30.9 eV. The interband transition spectra are very similar for both quartz and  $\text{AlPO}_4$ ; the four main transition peaks at 10.4, 11.4, 14.2, and 17.3 eV are essentially identical for both  $\text{AlPO}_4$  and *c*- $\text{SiO}_2$ , qualitatively agreeing with other reported optical transitions for crystalline silica [36,37]. Except for the transition strength intensity, the transition peaks or shoulders at 16.2, 22.5, 24.5, and 28.0 eV are at the same positions for both  $\text{AlPO}_4$  and quartz. Given the *iso*-structural relationship between  $\text{SiO}_2$  and  $\text{AlPO}_4$ , similar units of  $\text{SiO}_4$  and  $\text{PO}_4$  tetrahedrons, it is not surprising that the energy bands of  $\text{AlPO}_4$  are similar to quartz [38] but with a different band energy gap [35].

We calculated the bulk energy loss function ( $\text{ELF} = -\text{Im}[1/\varepsilon(\omega)]$ ) as well as the surface energy loss function ( $\text{ELF} = -\text{Im}[1/\varepsilon(\omega) + 1]$ ) for  $\text{AlPO}_4$  as shown in Fig. 3 using the interband transition strength (Fig. 2), determined from Kramers–Kronig analysis of the VUV reflectance spectrum. The bulk plasmon peak in the ELF spectrum of Fig. 3 for  $\text{AlPO}_4$  is estimated to be 23.7 eV, which is the same as amorphous  $\text{SiO}_2$  (23.7 eV), but not of crystalline  $\text{SiO}_2$  (24.6 eV and 25.2, respectively, for X- and Z-cut Quartz). The surface plasmon peak was expected to appear at  $23.7/\sqrt{2} = 16.4$  eV, and therefore we identify the peak in the surface energy loss function at 18.4 eV as arising from the surface plasmon. Therefore, the feature peaks at 21 eV and at lower energies are attributed to interband transitions. The bulk or surface plasmon energies can also be identified by the convention of locating the second zero crossing (or closest approach to zero if there is no zero crossing) of the real part of the dielectric constant ( $\varepsilon_1$ ), where  $\varepsilon_1$  exhibits a positive slope. This zero crossing will produce a maximum in

the energy loss function, and serves as another simple definition of the bulk or surface plasmon energy. But even this approach does not produce definitive results, when, as in  $\text{AlPO}_4$  there are strong interband transitions, which can give rise to multiple zero crossings, or multiple regions where  $\epsilon_1$  approaches very close to zero.

The expected value of the oscillator strength sum rule for  $\text{AlPO}_4$  is 32 electrons per  $\text{AlPO}_4$  per formula unit, consisting of 2 Al 3s electrons, 1 Al 3p electron, 16 O 2p electrons, 8 O 2s electrons, 2 P 3s electrons and 3 P 3p electrons. The oscillator-strength sum rule  $n_{\text{eff}}$  for  $\text{AlPO}_4$ , which was calculated from its interband transition strength spectrum, shown in Fig. 4, indicates that 19 electrons per formula unit participate in transitions at energies at or below 44 eV. As discussed by Smith [39] the fact that the sum rule at 44 eV shows 19 valence electron transitions represents that there is additional oscillator strength which has been spread into higher energy interband transitions.

### 3.2. Amorphous and crystalline silica

Differences in the amplitude of the reflectivity and the refractive index of crystalline and amorphous  $\text{SiO}_2$  [1] comes from the variation of the Si–O–Si angle in  $\text{SiO}_4$  tetrahedron and the orderly alignment of these tetrahedra. The quartz samples have much higher reflectance and refractive indices than amorphous silica predominantly due to the quartz's higher physical density [40]. There are also some differences among quartz and amorphous samples themselves. Z-cut quartz has a higher value of the reflectance and refraction index than X-cut quartz. The short-range order (SRO) of amorphous  $\text{SiO}_2$  is the same as in the 4:2 coordinated crystals. However, it is the intermediate range order (IRO) and the lack of long-range order (LRO) that distinguished the a- $\text{SiO}_2$  from its crystalline counterpart. The long-range order is destroyed on transition from the periodic crystalline lattice to the more random amorphous state. Therefore, the LRO and IRO make the interband transitions of crystalline  $\text{SiO}_2$  exhibit sharper features than does the amorphous  $\text{SiO}_2$  counterpart (as shown in the interband transition strength in Fig. 5 for example at the band gap), whose LRO had been destroyed and whose valence and conduction bands are consequently broadened.

### 3.3. SiC

The interband transition strength ( $\text{Re}[J_{\text{cv}}]$ ) of 6H SiC is shown in Fig. 6. The experimentally determined complex dielectric function (Fig. 7) is compared with Ching's [41] first principles OLCAO calculation of the band structure and optical properties of 6H SiC. The experimental interband transition strength ( $J_{\text{cv}}$ ) spectrum shows features at 7.2, 7.51, 9.06, 9.2, 11.1, 16.9, 19.8 and 32.3 eV. The calculated band structure and optical properties of 6H SiC have been discussed in the literature, but clear transition assignments have not been reported [42]. A clear correspondence can be established between all the main interband transition features in experiment and theory. In 3C SiC, the main peak in the interband transitions has been assigned transitions of the upper two valence bands to the lowest conduction band [43].

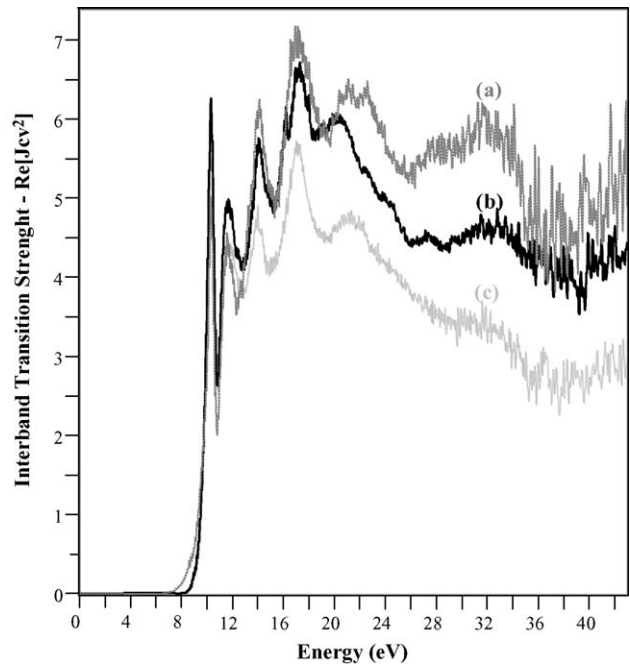


Fig. 5. Real part of the interband transition strength ( $\text{Re}[J_{\text{cv}}]$ ) of (a) X-cut Quartz, (b) Z-cut Quartz, and (c) a- $\text{SiO}_2$  determined from Kramers–Kronig analysis of VUV reflectance data.

### 3.4. $\text{Si}_3\text{N}_4$

We have previously studied [44] the interband transitions of  $\text{Si}_3\text{N}_4$  using both VUV spectroscopy and V-TEELS to determine the interband transition strength of silicon nitride, and to compare the two experimental methods. The electronic structure of  $\text{Si}_3\text{N}_4$  is quite different from the forms of  $\text{SiO}_2$  shown here.

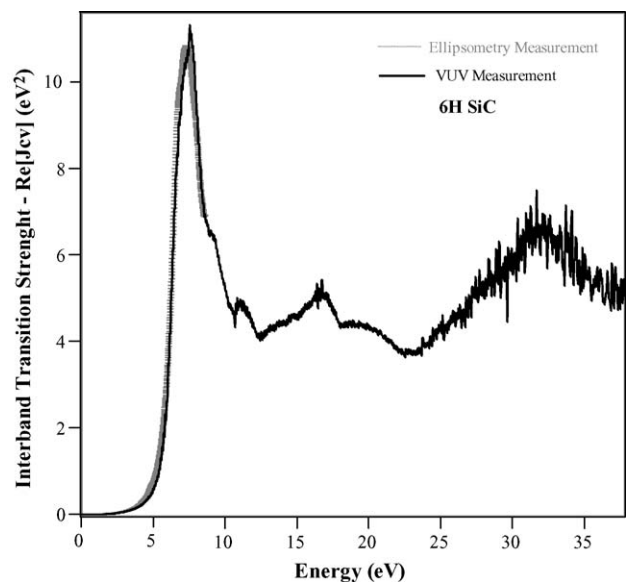


Fig. 6. Interband transition strength spectrum ( $\text{Re}[J_{\text{cv}}]$ ) of 6H SiC (black line), derived from Kramers–Kronig analysis of VUV reflectance data. In addition the reflectance as calculated from spectroscopic ellipsometry below 8 eV is shown as the wide grey line.

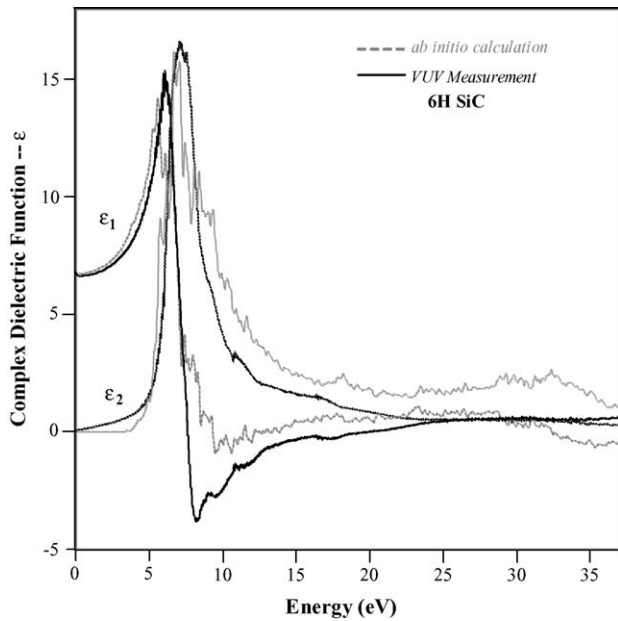


Fig. 7. Complex Dielectric Function of 6H SiC from VUV spectroscopy (black line) and an ab initio LDA band structure calculation of Ching [41].

### 3.5. SiON glasses

In  $\text{Si}_3\text{N}_4$  structural ceramics, oxynitride glass films form at the grain interfaces, and the doping of these with Mg or Al or rare-earth additives is used to design and control the room temperature or high temperature mechanical properties. Therefore, knowledge of the optical properties and Hamaker constants involving these glasses is of importance. We have studied a variety of SiON glasses whose properties are in some manner intermediate between the nitride and the oxide of silicon, modified by the dopants in the glass. The composition of the YMg and LuMg SiON glasses are listed in Table 1, where one can see that the composition of the two YMg samples are slightly different. These compositional changes and their effects on the interband transitions can be seen in Fig. 8 and also in the changes in the indices of refractions of the glasses reported in Table 1.

### 3.6. $\text{SrTiO}_3$ and its grain boundaries

We have studied the electronic structure of  $\text{SrTiO}_3$  [7] using ab initio methods and VUV spectroscopy and V-TEELS [14]. We have also studied changes in the electronic structure and optical properties of  $\text{SrTiO}_3$  due to non-stoichiometry from oxidation and reduction [45]. Most recently [46] we have used V-TEELS for  $\Sigma 5$  and near  $\Sigma 13$  grain boundaries in Fe doped  $\text{SrTiO}_3$ .

Table 1

Composition of SiON glasses, in at.% [55], and the index of refraction determined from analysis of the VUV reflectance, and the  $A_{121}$  Hamaker constant for the SiON glass between two grains of  $\text{Si}_3\text{N}_4$

Si	M	Re	O	N	Sample ID	Index of refraction	$A_{121}$ Hamaker constant (zJ)
19.2	12.77	8.51	51.06	8.51	SiMgYON851	1.78	4.54
19.2	12.82	8.55	50	9.4	SiMgYON855	1.71	6.50
19.2	12.77	8.51	51.06	8.51	SiMgLUNON851	1.70	7.86

For comparison, the index of refraction of bulk  $\text{Si}_3\text{N}_4$  is 1.97 [3].

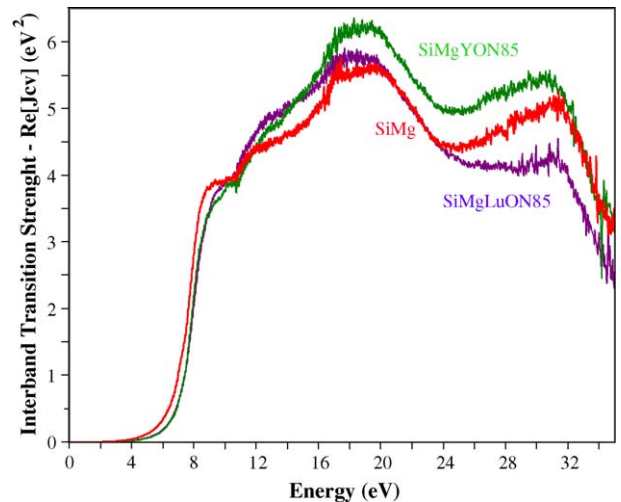


Fig. 8. Interband transition strength spectrum ( $\text{Re}[J_{cv}]$ ) of Mg containing RE-Mg-SiON glasses derived from Kramers–Kronig analysis of VUV reflectance data. The glasses are Mg containing glasses, 9537-SiMgYON851, 9538-SiMgYON855, 9540-SiMgLUNON851.

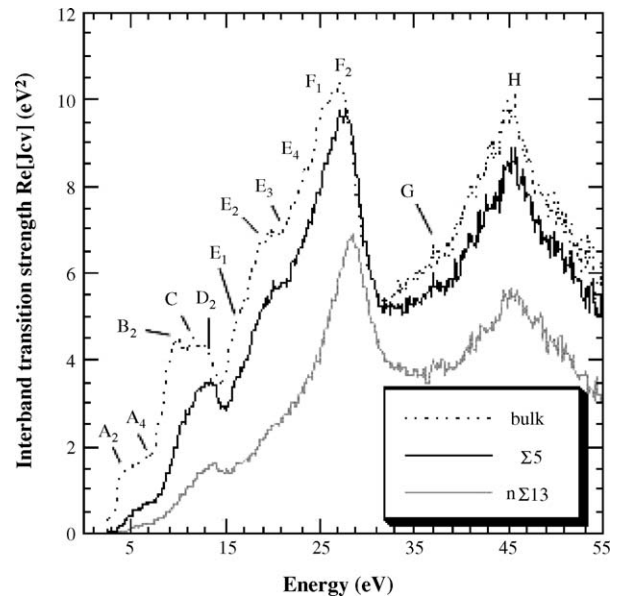


Fig. 9. Interband transition strength ( $\text{Re}[J_{cv}]$ ) determined from transmission valence electron energy loss spectroscopy (T-VEELS) for bulk  $\text{SrTiO}_3$ , for the  $\Sigma 5$  and the  $n\Sigma 13$  grain boundaries.

In Fig. 9 we show the interband transitions of bulk  $\text{SrTiO}_3$ , with the interband transition assignments as presented in Ref. [7], and then the interband transitions determined in situ with a 0.8 nm probe size in V-TEELS, in the grain boundary core.

The substantial changes in the electronic structure of the grain boundary core of these two grain boundaries demonstrate that the core can be considered as a “different” interlayer material, and we can therefore consider the Hamaker coefficient for these atomically structured grain boundaries.

## 4. Discussion

### 4.1. Experimental approaches for bulk and interfacial and surficial films

In the hierarchy of bulk material and interfacial and surficial materials, there have been great advances in methods to determine the optical properties and electronic structure of bulk materials using quantitative analysis of VUV spectroscopy [47] and of interfacial materials such as films or grain boundaries using quantitative analysis of V-TEELS [12]. The experimental methods have now become established and the quantitative analysis is broadly available in readily available software such as the Electronic Structure Tools (EST) [48].

The quantitative methods for optical properties and electronic structure information for surficial films is, relatively speaking, in its infancy. The use of V-REELS for surficial films and the developed bulk and interfacial methods shown here may be of aid to the surface science community or applied to critical surficial film problems such as the gate dielectric films in CMOS transistors. We are at the beginning of this surficial film topic, where we can now have Kramers–Kronig transforms for both the surface and the bulk energy loss function [13], and we can acquire V-REELS data. But the next step is the development of analytical models of the energy loss interactions at surfaces of bulk samples, and methods to simultaneously separate the bulk energy loss function and the surface energy loss function. Once this separation can be performed, we should be able to extract quantitative optical properties and electronic structure information for surficial films, and use the in situ V-REELS measurements to determine the London dispersion interactions in these systems. We will continue this effort, and will implement our techniques in EST for general use.

### 4.2. Interband transition strengths for important film forming systems

With our focus on nanostructured amorphous films in ceramic systems, it is of great importance to develop a broad knowledge of the complex optical properties and electronic structure of materials. It is both important to see which materials exhibit similar interband transitions and which are dissimilar. In addition, the effects of compositional changes, doping, and atomic structural changes on the interband transitions will be important as we try to understand what appreciable effects may arise in a low-dimensional constrained film of unique composition and structure at an interface or a free surface.

Consider the electronic structure and interband transitions of  $\text{AlPO}_4$ ,  $\text{SiO}_2$  Quartz, amorphous  $\text{SiO}_2$  and RE-MgSiON glasses as presented here. The interband transitions of  $\text{AlPO}_4$  and  $\text{SiO}_2$  are very closely related and arise from their analogous crystalline

structures. The crystalline and amorphous forms of  $\text{SiO}_2$  exhibit differences, for example in their index of refraction, which arise from changes in the atomic structure due to the disruption of long range order in the amorphous phase and a concomitant reduction in the physical density of amorphous  $\text{SiO}_2$  relative to Quartz. With the changes from  $\text{AlPO}_4$  to  $\text{SiO}_2$  producing not much change in the interatomic bonding, this suggests that the atomic structure (which is closely related for these three phases) plays an important role, while the chemistry plays a less important role in these systems.

Comparing  $\text{SiO}_2$  to SiC, one sees that the change of anion from O to C and the related change in atomic structure lead to dramatic differences in their electronic structures. It is interesting to note that the electronic structure of SiC and  $\text{Si}_3\text{N}_4$  are more closely related than either is to  $\text{SiO}_2$ . When we then consider the electronic structure of RE-MgSiON glasses synthesized to have compositions comparable to intergranular films in  $\text{Si}_3\text{N}_4$ , the optical properties are comparable to  $\text{Si}_3\text{N}_4$ , but the index of refraction is reduced. This reduction of the index of refraction in the intergranular glass determines and controls the magnitude of the attractive London dispersion interaction.

### 4.3. London dispersion interactions in these systems

The non-retarded Hamaker constant,  $A_{121}^{\text{NR}}$ , determines the magnitude of the London dispersion interaction between the two adjacent grains (material 1) separated by an interlayer (material 2) of width  $L$ , in the non-retarded limit of small interlayer thickness:

$$A_{121}^{\text{NR}} = -6\pi L^3 F_{\text{London}} = -12\pi L^2 E_{\text{London}} \quad (20)$$

These dispersion interactions can be represented by the Hamaker constant (a constant in the non-retarded limit) or the Hamaker coefficient (which varies with the separation distance) or by the London dispersion force or energy if a separation is defined. The Hamaker coefficient can be determined from the complex optical properties, as presented here, or it can be determined using various approximations or by analysis of surface energies, or atomic force microscope force distance relations. We have discussed these contrasting approaches to dispersion interactions previously [49]. The role that London dispersion interaction and interfacial amorphous films play in materials properties can be seen in chip resistors [50] and in  $\text{Si}_3\text{N}_4$  structural ceramics [44].

#### 4.3.1. Interfacial films in silicon nitride

The Hamaker constants  $A_{121}$  for the configuration of two  $\text{Si}_3\text{N}_4$  grains separated by an interlayer of the Re (=Lu, Y) doped SiMgON glasses is shown in Table 1. When the change in the  $A_{121}$  Hamaker constant is considered against the index of refraction of the interlayer SiON glass it is observed that the Hamaker constant decreases almost linearly with increasing index of refraction of the intergranular film. The index of refraction for the different glasses and the corresponding Hamaker constants both show a clear dependence on the composition of the glasses.

Table 2  
Hamaker coefficients of the London dispersion interaction for grain boundaries in SrTiO<sub>3</sub> [46]

Interface	Abrupt gradient		Double-quadratic gradient	
	$A_{121}^{NR}$ (zJ)	$E_{London}$ (mJ m <sup>-2</sup> )	$A_{121}^{NR}$ (zJ)	$E_{London}$ (mJ m <sup>-2</sup> )
SrTiO <sub>3</sub>  vac. SrTiO <sub>3</sub> ( $d_0 = 0.195$ nm)	243.9	169	171.2 ( $L = 0.9$ nm)	119
SrTiO <sub>3</sub>   $n\Sigma 13$  SrTiO <sub>3</sub> ( $d_0 = 0.195$ nm)	105.5	73	72.5 ( $L = 0.9$ nm)	50
SrTiO <sub>3</sub>   $\Sigma 5$  SrTiO <sub>3</sub> ( $d_0 = 0.195$ nm)	35.0	24	20.7 ( $L = 0.6$ nm)	14
SiO <sub>2</sub>  vac. SiO <sub>2</sub> ( $d_0 = 0.165$ nm)	68.2	66	50.3	49

These Hamaker constants are comparable to prior work on LaAlSiON glass Si<sub>3</sub>N<sub>4</sub> determined from T-VEELS spectrum [44]. The Hamaker constant ( $A_{121}$ ) for the configuration of (Si<sub>3</sub>N<sub>4</sub>|LaAl-glass|Si<sub>3</sub>N<sub>4</sub>) averaged at 8.3 zJ, and showed variations among different interfaces of 2.0–12.6 zJ. VUV spectroscopy found a Hamaker constant of 2.72 zJ which may be lower, due to assumptions on the bulk glass composition that corresponds to the intergranular film composition. The Hamaker constant ( $A_{121}$ ) for the configuration of (Si<sub>3</sub>N<sub>4</sub>|YAl-glass|Si<sub>3</sub>N<sub>4</sub>) averaged 9.3 zJ, and was close to the value of 6.5 zJ determined from VUV spectrum of bulk samples (Si<sub>3</sub>N<sub>4</sub>|YM-glass|Si<sub>3</sub>N<sub>4</sub>) reported here.

#### 4.3.2. London dispersion interactions in SrTiO<sub>3</sub> grain boundaries

Full spectral Hamaker constants and London dispersion energies for atomic grain boundaries in SrTiO<sub>3</sub>, shown in Table 2, were determined based on the three-layer model and the interband transition strength spectra of Fig. 9. The positive value of  $A_{121}^{NR}$  constants reveals the existence of attractive London dispersion forces across the grain boundaries with the boundary core serving as an “interfacial layer” of a unique material between the grains. The limiting values for the Hamaker constant for differing interfacial layer properties would be a maximum for a vacuum interlayer and zero if the interfacial layer were indistinguishable from the bulk. Since the optical contrast for the  $n\Sigma 13$  GB is bigger than that of  $\Sigma 5$ , its London dispersion force is larger.

For more complex grain boundary structures the use of the three-layer model for the dispersion interaction is no longer suitable since properties vary continuously across the grain boundary core. Therefore, we used our multilayer model for calculating full spectral retarded Hamaker coefficients for graded interfaces. We can more realistically model the  $\Sigma 5$  and  $n\Sigma 13$  SrTiO<sub>3</sub> grain boundary structures using the maximal core width perpendicular to the boundary plane of 0.6 nm [51] and 0.9 nm [52], respectively. In addition, a region adjacent to the boundary core was chosen, in which a double quadratic gradient of the complex optical properties serves as a continuous transition between the bulk and the boundary core, with a thickness of  $d_0 = 0.195$  nm, corresponding to a Ti–O bond length in SrTiO<sub>3</sub>. The local properties were scaled on the basis of a double-quadratic function as shown in Fig. 10. Resulting Hamaker coefficient and London dispersion interaction energies for the given core thickness are shown in Table 2. London dispersion interaction energies

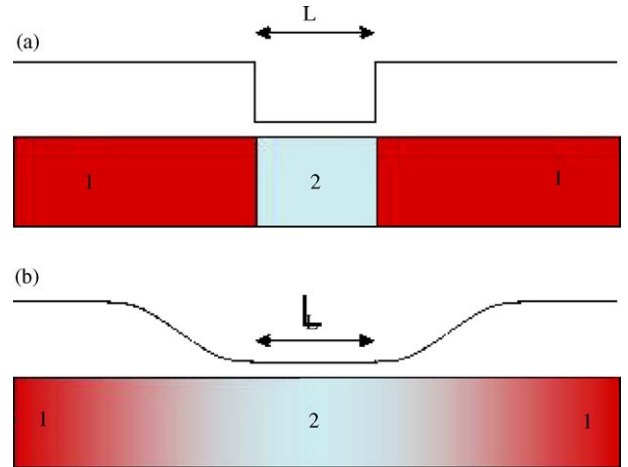


Fig. 10. Sketch view of the single layer (a) and multilayer model (b) to determine Hamaker constants of interfaces with graded structures.

are 169 and 119 mJ/m<sup>2</sup> for the three-layer and the multilayer model, respectively, if the boundary core is essentially vacuum. These energies are appreciable and of the order of 10% of surface energies for SrTiO<sub>3</sub> [53,54]. The graded-interface model leads to only a small reduction in the calculated magnitude of the London dispersion interaction at the investigated SrTiO<sub>3</sub> grain boundaries.

## 5. Conclusions

Nanostructured amorphous films exhibit complex thermodynamic and kinetic behavior. To understand the structure and properties of nanostructured amorphous films in silicon based ceramics (Si<sub>3</sub>N<sub>4</sub>, SiC, Si) and in SrTiO<sub>3</sub> ceramics we have focused on experimental studies to determine the interband electronic structure and optical properties. We use vacuum ultraviolet spectroscopy for bulk materials, and valence electron energy loss spectroscopy in either transmission mode in the transmission electron microscope for interfacial films, or in reflection mode for surficial films. These experimental data are quantitatively analyzed using Kramers–Kronig analysis to determine the complex optical properties of the materials. This interband electronic structure information is the fundamental input to determine from Lifshitz theory the London dispersion interaction in these low-dimensional systems. We present interband transition

strengths of  $\text{AlPO}_4$ ,  $\text{SiO}_2$  and rare-earth doped  $\text{MgSiON}$  glasses, and also of  $\text{SiC}$  and  $\text{SrTiO}_3$  and its grain boundaries. We use a multilayer approach to produce graded interface models for the London dispersion interaction in complex nanostructured interfacial and surficial films.

## Acknowledgements

We would like to thank R.D. Shannon for the  $\text{AlPO}_4$  crystal, and R. Satet and M. Hoffmann for the  $\text{SiON}$  glass samples. We are grateful to M.F. Lemon and M.K. Yang for assistance with spectroscopy and ellipsometry, Dr. L.K. Denoyer for software development, and B.B. French for editing the manuscript. This work was partially funded by NSF Award DMR-0010062 in cooperation with EU Commission Contract G5RD-CT-2001-00586.

## References

- [1] G.L. Tan, M.F. Lemon, R.H. French, *J. Am. Ceram. Soc.* 86 (2003) 1885–1892.
- [2] R.H. French, H. Müllejans, D.J. Jones, G. Duscher, R.M. Cannon, M. Rühle, *Acta Mater.* 46 (1998) 2271–2287.
- [3] Y.N. Xu, W.Y. Ching, R.H. French, *Phys. Rev. B* 48 (1993) 17695.
- [4] R.H. French, S.J. Glass, F.S. Ohuchi, Y.-N. Xu, F. Zandiehnam, W.Y. Ching, *Phys. Rev. B* 49 (1994) 5133.
- [5] R.H. French, D.J. Jones, S. Loughin, *J. Am. Ceram. Soc.* 77 (1994) 412.
- [6] R.H. French, J.B. Blum, *Ceramic Transactions*, vol. 7, American Ceramics Society, Westerville, OH, 1990, p. 111.
- [7] K. van Benthem, C. Elsässer, R.H. French, *J. Appl. Phys.* 90 (2001) 6156.
- [8] M.L. Bortz, R.H. French, *Appl. Phys. Lett.* 55 (19) (1989) 1955–1957.
- [9] R.H. French, *Phys. Scrip.* 41 (4) (1990) 404–408.
- [10] R.H. French, *J. Am. Ceram. Soc.* 73 (3) (1990) 477–489.
- [11] R.H. French, D.J. Jones, S. Loughin, *J. Am. Ceram. Soc.* 77 (1994) 412–422.
- [12] A.D. Dorneich, R.H. French, H. Müllejans, S. Loughin, M. Rühle, *J. Microsc.* 191 (1998) 286.
- [13] G.L. Tan, L.K. DeNoyer, R.H. French, M.J. Guittet, M. Gautier-Soyer, *J. Electr. Spectrosc. Relat. Phenom.* 142 (2004) 97–103.
- [14] K. van Benthem, R.H. French, W. Sigle, C. Elsässer, M. Rühle, *Ultramicroscopy* 86 (3/4) (2001) 303–318.
- [15] G.L. Tan, L.K. Denoyer, R.H. French, A. Ramos, M. Gautier-Soyer, Y.M. Chiang, *MRS Proceedings on Fundamentals of Novel, Oxide/Semiconductor Interfaces*, 2004, p. E1.9.1.
- [16] F. Wooten, *Optical Properties of Solids*, Academic Press, New York, 1972, p. 49.
- [17] P.J. Mohr, B.N. Taylor, *CODATA Recommended Values of the Fundamental Physical Constants: 1998*, National Institute of Standards and Technology, Gaithersburg, MD, USA or visit <http://physics.nist.gov/constants/>.
- [18] R. de L. Kronig, *J. Opt. Soc. Am.* 12 (1926) 547–557.
- [19] C.J. Gorter, R. de L. Kronig, *Physica III* 9 (1936) 1009–1020.
- [20] H.A. Kramers, *Atti. Congr. Intern. Fis. Como.* 2 (1927) 545–557.
- [21] M.L. Bortz, R.H. French, *Appl. Spectrosc.* 43 (8) (1989) 1498–1501.
- [22] R.H. French, D.J. Jones, H. Müllejans, S. Loughin, A.D. Dorneich, P.F. Garcia, *J. Mater. Res.* 14 (1999) 4337–4344.
- [23] J. Daniels, C. von Festenberg, H. Raether, K. Zeppenfeld, in: G. Hoehler (Ed.), *Tracks in Modern Physics*, vol. 54, Springer, New York, 1970.
- [24] R.F. Egeron, *Electron Energy Loss Spectroscopy in the Electron Microscope*, Plenum, New York, 1986.
- [25] J. Plueger, J. Fink, W. Webre, K.P. Bohnen, *Phys. Rev. B* 31 (1985) 1244.
- [26] R.H. Ritchie, A. Howie, *Philos. Mag.* A 36 (1977) 463–481.
- [27] P. Schattschneider, *Fundamentals of Inelastic Electron Scattering*, Springer, Wien, 1986.
- [28] D.Y. Smith, in: E.D. Palik (Ed.), *Handbook of Optical Constants of Solids*, Academic Press, New York, 1985, pp. 35–68.
- [29] E. Shiles, T. Sasaki, M. Inokuti, D.Y. Smith, *Phys. Rev. B* 22 (1980) 1612–1626.
- [30] R.H. French, *J. Am. Ceram. Soc.* 83 (9) (2000) 2117–2146.
- [31] E.M. Lifshitz, *Soviet Phys. JETP* 2 (1956) 73.
- [32] I.E. Dzyaloshinskii, E.M. Lifshitz, L.P. Pitaevskii, *Adv. Phys.* 10 (38) (1961) 165–209.
- [33] B.W. Ninham, V.A. Parsegian, *J. Chem. Phys.* 52 (1970) 4578–4587.
- [33a] R. Podgornik, R.H. French, V.A. Parsegian, *J. Chem. Phys.* 124 (2006), 044709.
- [34] N. Thong, D. Schwarzenbach, *Acta Cryst.* A 35 (1979) 658.
- [35] G.L. Tan, M.F. Lemon, R.H. French, D.J. Jones, *J. Chem. Phys.*, submitted for publication.
- [36] H.R. Philipp, *J. Non-Crystal. Solids* 8–10 (1972) 627–632.
- [37] H.R. Philipp, *J. Phys. Chem. Solids* 32 (1971) 1935–1945.
- [38] D.M. Christie, N. Troullier, J.R. Chelikowsky, *Solid State Commun.* 98 (1996) 923.
- [39] D.Y. Smith, in: E.D. Palik (Ed.), *Handbook of Optical Constants of Solids*, Academic Press, New York, 1985, pp. 35–68.
- [40] G.L. Tan, M.F. Lemon, R.H. French, D.J. Jones, *Phys. Rev. B* 72 (2005), 205117.
- [41] G. L. Tan, M. F. Lemon, R. H. French, D. J. Jones, *Phys. Rev. B* 72 (2005) 2005117.
- [42] R.T.M. Ummels, P.A. Bobert, W. Van Haeringen, *Phys. Rev. B* 58 (1998) 6795–6799.
- [43] W.R.L. Lambrecht, B. Segall, W. Suttrop, M. Yonagathan, R.P. Devaty, W.J. Choyke, J.A. Edmond, J.A. Powell, M. Alouani, *Appl. Phys. Lett.* 63 (1993) 2747.
- [44] R.H. French, H. Müllejans, D.J. Jones, G. Duscher, R.M. Cannon, M. Rühle, *Acta Mater.* 46 (7) (1998) 2271–2287.
- [45] A. Frye, R.H. French, D.A. Bonnell, *Z. Metallkd.* 94 (2003) 3.
- [46] K. van Benthem, G.L. Tan, L.K. Denoyer, R.H. French, M. Rühle, *Phys. Rev. Lett.* 93 (2004) 227201.
- [47] R.H. French, *J. Am. Ceram. Soc.* 73 (3) (1990) 477–489.
- [48] The electronic Structure Tools (EST) consists of a number of programs for the quantitative analysis of optical, VUV and EELS spectra. It has been developed under Grams, a PC based spectroscopy environment. EST is available from Deconvolution and Entropy Consulting, Ithaca, NY, or <http://www.deconvolution.com/>.
- [49] H.D. Ackler, R.H. French, Y.M. Chiang, *J. Colloid Interface Sci.* 179 (1996) 460–469.
- [50] Y.M. Chiang, L.E. Silverman, R.H. French, R.M. Cannon, *J. Am. Ceram. Soc.* 77 (1994) 1143–1152.
- [51] N.D. Browning, S.J. Pennycook, *J. Phys. D: Appl. Phys.* 29 (1996) 1779.
- [52] S. Hutt, O. Kienzle, F. Ernst, M. Rühle, *Z. Metallkd.* 92 (2001) 105.
- [53] J. Padilla, D. Vanderbilt, *Surf. Sci.* 418 (1998) 64.
- [54] T. Ochs, S. Koestlmeier, C. Elsässer, *Integrat. Ferroelectr.* 32 (2001) 959.
- [55] R. Satet, M. Hoffmann, Univ. Karlsruhe.